

Anisotropic adaptive finite element method for magnetohydrodynamic flow at high Hartmann numbers*

Jikun ZHAO¹, Shipeng MAO^{2,3,†}, Weiyang ZHENG^{2,3}

1. School of Mathematics and Statistics, Zhengzhou University, Zhengzhou 450001, China;
2. State Key Laboratory of Scientific and Engineering Computing (LSEC) and Institute of Computational Mathematics, Academy of Mathematics and Systems Science (AMSS), Chinese Academy of Sciences, Beijing 100190, China;
3. School of Mathematical Sciences, University of Chinese Academy of Sciences, Beijing 100190, China

Abstract This paper presents an anisotropic adaptive finite element method (FEM) to solve the governing equations of steady magnetohydrodynamic (MHD) duct flow. A residual error estimator is presented for the standard FEM, and two-sided bounds on the error independent of the aspect ratio of meshes are provided. Based on the Zienkiewicz-Zhu estimates, a computable anisotropic error indicator and an implement anisotropic adaptive refinement for the MHD problem are derived at different values of the Hartmann number. The most distinguishing feature of the method is that the layer information from some directions is captured well such that the number of mesh vertices is dramatically reduced for a given level of accuracy. Thus, this approach is more suitable for approximating the layer problem at high Hartmann numbers. Numerical results show efficiency of the algorithm.

Key words magnetohydrodynamic (MHD) flow, posteriori error estimate, anisotropic adaptive finite element method (FEM)

Chinese Library Classification O242.21

2010 Mathematics Subject Classification 65N15, 65N30

1 Introduction

The flow problem of viscous, incompressible, electrically conducting fluids in the channels and ducts under a uniform oblique magnetic field is of great interest, because it has many practical applications in the field of magnetohydrodynamics (MHD), such as the blood flow control and measurements, MHD flowmeters, MHD power generation, and accelerators. Only for some very special cases, the problem can be exactly solved. Therefore, for the sake of

* Received Jan. 25, 2016 / Revised Jun. 6, 2016

Project supported by the National Natural Science Foundation of China (Nos. 11471329, 11321061, and 91430215), the National Magnetic Confinement Fusion Science Program of China (No. 2015GB110000), the Youth Innovation Promotion Association of Chinese Academy of Sciences (CAS) (No. 2016003), and the National Center for Mathematics and Interdisciplinary Sciences of CAS

† Corresponding author, E-mail: maosp@lsec.cc.ac.cn

application, an effective numerical method to solve the MHD flow problem becomes an very important research topic.

It is well-known that, for large values of the Hartmann number, the MHD flow problem is convection-dominated such that the exact solution may display localized phenomena, such as interior or boundary layers. For solving the MHD flow problem, there have been many research works using various numerical methods, such as the finite element, finite difference, and boundary element methods. The readers can refer to Refs. [1]–[2] and many references cited therein. Unfortunately, because of the lack of stability or accuracy, most of conventional numerical methods cannot solve the layer problems efficiently. In Ref. [1], it was pointed out that the common deficiency among the existing numerical methods is that they produce accurate results only in several special configurations for the MHD duct flow problems, but the Hartmann number Ha cannot exceed about 10^2 . However, in many industrial applications, the important range of the Hartmann number is $10^2 < Ha < 10^6$. For this reason, some seemingly robust numerical methods with large Hartmann numbers were suggested, such as the stabilized finite element method (FEM)^[1] and least-squares FEM^[2] using residual-free bubble functions. Even so, for large Hartmann numbers, some spurious oscillations still appear near the boundary layer regions when these two bubble-stabilized methods are used (see Refs. [1] and [2] or also the discussion on this in Ref. [3]). Later, a tailored finite point method was proposed^[3], and high accuracy was achieved even for large Hartmann numbers. Beyond that, the boundary elements method^[4] and the two-level element free Galerkin method^[5] were also presented for solving the MHD duct flow problem at high Hartmann numbers, respectively. The theoretical error analysis of these methods above remains seriously poor except for the least-squares FEM^[2]. In addition, those methods were only investigated on isotropic meshes where the aspect ratio of mesh elements was uniformly bounded.

For such layer problems, a special anisotropic mesh adaptivity is more desirable, i.e., the mesh elements should adapt in both size and shape in order to approximate the solution better. There have been a well-developed literature on a posteriori error estimation but on isotropic meshes (see Refs. [6] and [7] and the references therein). Some types of the posteriori error estimate have already been extended to anisotropic meshes with large aspect ratio by Kunert^[8–10], but no anisotropic mesh refinements were made. Due to large aspect ratio, there appears the alignment measure in a posteriori error estimation to quantify the alignment between the solution and the mesh, which is one of the most important contributions of Kunert.

Based on a priori error estimate, the concept of metrics was mostly used in anisotropic mesh adaptation^[11–12]. A priori error analysis on anisotropic meshes can be found in Refs. [13] and [14] and the references therein. Moreover, a posteriori error indicator was used in anisotropic mesh adaptation^[15]. The concept of metrics was combined with the solution of a dual problem and a posteriori error analysis in order to generate an adaptive mesh^[16]. The metric field was directly obtained from a posteriori error estimate and used in the anisotropic mesh adaptation^[17].

In this paper, we present an anisotropic adaptive FEM to solve the MHD duct flow problem in a straight channel of uniform cross-section. By the analytic tools of Kunert^[9], a residual error estimator is proposed and provides two-sided bounds on the error on anisotropic meshes. However, the error estimator is not available for anisotropic adaptive refinement, because it cannot represent the contributions to the whole error in different directions, and the alignment measure, in which the exact solution is contained, enters the upper error bound. In order to use the alignment measure as a guide to design a proper anisotropic mesh, we reformulate its definition and use the well-known Zienkiewicz-Zhu (Z-Z) estimates^[6]. Then, a computable anisotropic error indicator is derived, and the corresponding locally error indicators are used to adjust the mesh sizes in different directions. Note that an analogous error indicator was proposed for anisotropic adaptive refinement for elliptic and parabolic problems in Ref. [15]. Finally, we implement an adaptive algorithm using the software FREEFEM++^[18] with the

mesh generator Bamg^[19] based on a right metric field obtained by the locally error estimates and Z-Z estimates of the error gradient matrix. By this method, the layer information from some directions can be well captured such that the number of mesh vertices is dramatically reduced for a given level of accuracy. Numerical results confirm the error analysis.

The paper is organized as follows. We first specify our notation and give some preliminary results in Section 2. Section 3 is devoted to analytical tools, such as inverse inequalities, alignment measure, and anisotropic interpolation estimates. An error estimator is proposed for the MHD problem, and the two-sided bounds on the error are derived on anisotropic meshes in Section 4. In Section 5, we derive an anisotropic error indicator and implement an adaptive algorithm. Therein, a series of numerical simulations for three test problems at different Hartmann numbers are carried out to demonstrate effectiveness of the anisotropic adaptive FEM.

2 Preliminaries

In this section, we give some notation and the anisotropic mesh description, present some preliminary results, and finally introduce the model problem and its conforming discretization.

2.1 Notation

For a bounded domain Ω with the Lipschitz continuous boundary $\partial\Omega$, let S be any given open subset of Ω . For the spaces $L^2(S)$ and $L^2(S)^2$, the integral inner product and the norm are denoted by $(\cdot, \cdot)_S$ and $\|\cdot\|_S$, respectively. If $S = \Omega$, the subscript will be omitted. Let $|S|$ be the Lebesgue measure of S , and in particular, $|s|$ is the length of a segment s . $\mathcal{P}_k(S)$ is the space of polynomials of order k or less, where k is a given non-negative integer. For simplicity, instead of $x \leq cy$ and $c_1x \leq y \leq c_2x$, we use the abbreviated notation $x \lesssim y$ and $x \sim y$, where the constants c, c_1 , and c_2 are independent of x, y , the Hartmann number, and the mesh.

By $\mathcal{F} = \{\mathcal{T}_h\}$, we denote a family of triangulations \mathcal{T}_h of Ω , where any two triangles are either disjoint or share a common vertex or edge. Let \mathcal{E}_h be the set of all edges of \mathcal{T}_h , let $\mathcal{E}_h^{\text{int}}$ be the set of interior, and let $\mathcal{E}_h^{\text{ext}}$ be the set of boundary. We denote by \mathcal{N}_h ($\mathcal{N}_h^{\text{int}}, \mathcal{N}_h^{\text{ext}}$) the set of all (interior, boundary) vertices of \mathcal{T}_h . Define for $a \in \mathcal{N}_h$, $\sigma \in \mathcal{E}_h$, and $K \in \mathcal{T}_h$, $\mathcal{T}_a := \{L \in \mathcal{T}_h; a \in L\}$, $\mathcal{T}_\sigma := \{L \in \mathcal{T}_h; \sigma \subset L\}$, and $\mathcal{T}_K := \{L \in \mathcal{T}_h; L \cap K \neq \emptyset\}$, respectively. Furthermore, three auxiliary subdomains need to be defined by

$$\omega_a := \cup\{L \in \mathcal{T}_a\}, \quad \omega_\sigma := \cup\{L \in \mathcal{T}_\sigma\}, \quad \omega_K := \cup\{L \in \mathcal{T}_K\}.$$

Next, the notation \mathbf{n}_K always denotes the exterior unit normal vector for any given $K \in \mathcal{T}_h$, and \mathbf{n}_σ denotes the unit normal vector for any given edge $\sigma \in \mathcal{E}_h$, of which the orientation is arbitrarily chosen but coinciding with the exterior normal of the domain Ω for boundary edges and fixed for interior edges.

For a function φ and an edge $\sigma \in \mathcal{E}_h^{\text{int}}$ shared by two triangles K and L , where \mathbf{n}_σ points from K to L , we define the jump operator $[[\cdot]]$ through σ by

$$[[\varphi]] := (\varphi|_K)|_\sigma - (\varphi|_L)|_\sigma.$$

For any $\sigma \in \mathcal{E}_h^{\text{ext}}$, set $[[\varphi]] := \varphi|_\sigma$.

2.2 Anisotropic meshes

For an arbitrary (anisotropic) triangle $K \in \mathcal{T}_h$, we enumerate its vertices such that P_0P_1 is the longest edge and $|P_1P_2| \geq |P_0P_2|$. Moreover, we define two orthogonal vectors \mathbf{p}_i with the length $h_{i,K} := |\mathbf{p}_i|$ ($i = 1, 2$), as shown in Fig. 1. Notice that $h_{1,K} \geq h_{2,K}$, set $h_{\min,K} := h_{2,K}$, and $h_{\max,K} := h_{1,K}$. For $\sigma \subset \partial K$, let

$$h_{\sigma,K} := \frac{2|K|}{|\sigma|}.$$

Define two 2×2 matrices \mathbf{A}_K and \mathbf{C}_K by

$$\mathbf{A}_K := (P_0 P_1, P_0 P_2), \quad \mathbf{C}_K := (\mathbf{p}_1, \mathbf{p}_2).$$

Additionally, we require that the mesh \mathcal{T}_h satisfies the following requirements:

(i) The number of triangles contained in \mathcal{T}_a is bounded uniformly for each fixed vertex $a \in \mathcal{N}_h$.

(ii) The dimension of adjacent triangles is close to each other, i.e.,

$$h_{i,K} \sim h_{i,L}, \quad K \cap L \neq \emptyset, \quad i = 1, 2.$$

For convenience, for the common edge σ shared by two triangles K and L , set

$$h_\sigma := \frac{h_{\sigma,K} + h_{\sigma,L}}{2}, \quad h_{\min,\sigma} := \frac{h_{\min,K} + h_{\min,L}}{2}.$$

An advantage of doing this is that they are no longer related to either of K or L but only to σ . For the boundary edges, the definitions are changed in the obvious way. Obviously, they satisfy $h_\sigma \sim h_{\sigma,K} \sim h_{\sigma,L}$ and $h_{\min,\sigma} \sim h_{\min,K} \sim h_{\min,L}$. For more details on anisotropic meshes, see Refs. [8] and [9].

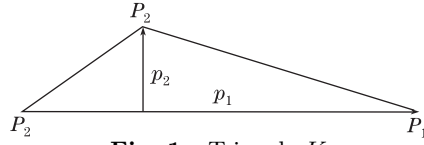


Fig. 1 Triangle K

2.3 Definition of problem and its conforming discretization

In a straight channel of a uniform cross-section Ω , we assume that there exists a laminar fully developed flow of a viscous, incompressible, and electrically conducting fluid. Let u be the velocity, and let B be the induced magnetic field. Here, the direction of the uniform transverse applied magnetic field B_0 may be arbitrary to the x -axis, and the fields u and B are parallel to the z -axis. Further, The fluid is driven down by a constant pressure gradient. The governing equations for the above duct flow in a dimensionless form with suitable boundary conditions can be posed as follows^[4,20]:

$$\begin{cases} -\Delta u - Ha \mathbf{a} \cdot \nabla B = 1 & \text{in } \Omega, \\ -\Delta B - Ha \mathbf{a} \cdot \nabla u = 0 & \text{in } \Omega, \\ u = 0 & \text{on } \partial\Omega, \\ B = 0 & \text{on } \Gamma_D, \\ \frac{\partial B}{\partial \mathbf{n}} = 0 & \text{on } \Gamma_N, \end{cases} \quad (1)$$

where $Ha = B_0 l (\delta/\nu)^{1/2}$ is the Hartmann number, l is the characteristic length of the duct, B_0 is the intensity of the external magnetic field, and ν and δ are the viscosity coefficient and electric conductivity of the fluid, respectively. $\mathbf{a} = (\cos \alpha, \sin \alpha)^T$, where α is the angle between the x -axis and the externally applied magnetic field B_0 . $\partial\Omega = \Gamma_D \cup \Gamma_N$, where $\Gamma_D \cap \Gamma_N = \emptyset$ and Γ_D has a positive measure. We call Γ_N the conducting part and Γ_D the insulated part of the boundary $\partial\Omega$.

Let $W_{0B}(\Omega) := H_0^1(\Omega) \times H_B^1(\Omega)$, where two particular subspaces of $H^1(\Omega)$ are

$$H_0^1(\Omega) := \{v \in H^1(\Omega); v|_{\partial\Omega} = 0\},$$

$$H_B^1(\Omega) := \{Q \in H^1(\Omega); Q|_{\Gamma_D} = 0\}.$$

Due to the Poincaré inequality, the space $W_{0B}(\Omega)$ will be equipped with the product norm,

$$\|(v, Q)\|_W := (\|\nabla v\|^2 + \|\nabla Q\|^2)^{1/2}, \quad (v, Q) \in W_{0B}(\Omega).$$

The weak form of the problem (1) is to find $(u, B) \in W_{0B}(\Omega)$ such that

$$(\nabla u, \nabla v) - Ha(\mathbf{a} \cdot \nabla B, v) + (\nabla B, \nabla Q) - Ha(\mathbf{a} \cdot \nabla u, Q) = (1, v), \quad \forall (v, Q) \in W_{0B}(\Omega). \quad (2)$$

In order to define the finite element approximation, let $V^h(\Omega)$ be a subspace of $H^1(\Omega)$ consisting of continuous piecewise affine functions on the mesh \mathcal{T}_h , and

$$W_{0B}^h(\Omega) := (V^h(\Omega) \cap H_0^1(\Omega)) \times (V^h(\Omega) \cap H_B^1(\Omega)).$$

Then, the standard FEM is to find $(u_h, B_h) \in W_{0B}^h(\Omega)$ such that

$$\begin{cases} (\nabla u_h, \nabla v_h) - Ha(\mathbf{a} \cdot \nabla B_h, v_h) + (\nabla B_h, \nabla Q_h) - Ha(\mathbf{a} \cdot \nabla u_h, Q_h) \\ = (1, v_h), \quad \forall (v_h, Q_h) \in W_{0B}^h(\Omega). \end{cases} \quad (3)$$

The existence and uniqueness of solutions to (2) and (3) can be easily obtained by the well-known Lax-Milgram lemma. A priori error analysis can be found in Ref. [21].

3 Analytical tools

In order to treat anisotropic elements, some analytical tools in the anisotropic setting have to be introduced here, which are taken from Refs. [8] and [9].

3.1 Inverse inequalities

Inverse inequalities for bubble functions are very important in deriving lower error bounds. As usual, we first introduce the bubble functions^[7]. For an arbitrary triangle K , denote the barycentric coordinates by $\lambda_{K,1}, \lambda_{K,2}$, and $\lambda_{K,3}$. We define the element bubble function b_K by

$$b_K := 27\lambda_{K,1}\lambda_{K,2}\lambda_{K,3} \quad \text{on } K.$$

Let σ be an inner edge shared by K_1 and K_2 . We here enumerate all the vertices of K_1 and K_2 such that the two vertices of σ are first numbered. We define the edge bubble function b_σ by

$$b_\sigma := 4\lambda_{K_i,1}\lambda_{K_i,2} \quad \text{on } K_i \quad (i = 1, 2).$$

Obvious modifications need to be done for boundary edges. For simplicity, b_K and b_σ are assumed to be extended by zero outside their original domain of definition.

For a given edge σ of a triangle K , an extension operator $F_{\text{ext}} : \mathcal{P}_0(\sigma) \rightarrow \mathcal{P}_0(K)$ is defined as follows:

$$F_{\text{ext}}(\varphi)(x) := \varphi|_\sigma \equiv \text{const.}$$

By standard scaling arguments, we can easily derive the following anisotropic inverse inequalities.

Lemma 1 *Assume that $\varphi_K \in \mathcal{P}_0(K)$ and $\varphi_\sigma \in \mathcal{P}_0(\sigma)$, where $\sigma \subset \partial K$. Then,*

$$\begin{aligned} \|b_K^{1/2}\varphi_K\|_K &\sim \|\varphi_K\|_K, \\ \|\nabla(b_K\varphi_K)\|_K &\lesssim h_{\min,K}^{-1}\|\varphi_K\|_K, \\ \|b_\sigma^{1/2}\varphi_\sigma\|_\sigma &\sim \|\varphi_\sigma\|_\sigma, \\ \|F_{\text{ext}}(\varphi_\sigma)b_\sigma\|_K &\sim h_\sigma^{1/2}\|\varphi_\sigma\|_\sigma, \\ \|\nabla(F_{\text{ext}}(\varphi_\sigma)b_\sigma)\|_K &\lesssim h_\sigma^{1/2}h_{\min,K}^{-1}\|\varphi_\sigma\|_\sigma. \end{aligned}$$

3.2 Alignment measure and anisotropic interpolation estimates

From a heuristic point of view, if the (directional) derivative of the solution displays little change in some direction, in that direction, we should stretch the mesh elements. The better the alignment is between the anisotropic mesh and the anisotropy of solution, the more accurate the error estimates can be. All practical applications intuitively follow this concept. Next, we should introduce the alignment measure $m_1(v, \mathcal{T}_h)$ in order to quantify this alignment.

For $v \in H^1(\Omega)$ and a family of triangulations $\{\mathcal{T}_h\}$, the alignment measure $m_1 : H^1(\Omega) \times \{\mathcal{T}_h\} \rightarrow \mathbb{R}$ is defined by

$$m_1(v, \mathcal{T}_h) := \frac{\left(\sum_{K \in \mathcal{T}_h} h_{\min,K}^{-2} \|C_K^\top \nabla v\|_K^2 \right)^{1/2}}{\|\nabla v\|}. \tag{4}$$

The alignment measure has the following property:

$$1 \leq m_1(v, \mathcal{T}_h) \lesssim \max_{K \in \mathcal{T}_h} \frac{h_{\max,K}}{h_{\min,K}}.$$

The above property implies that, if the mesh \mathcal{T}_h is well aligned with an anisotropic function v , it leads to a small alignment measure. In practice, for sensible anisotropic meshes, one almost always obtains $m_1(v, \mathcal{T}_h) \sim 1$. In this paper, we should apply this property to anisotropic mesh adaption (see numerical experiments in Section 5).

Consider a node $a \in \mathcal{N}_h$. The local L^2 -projection $P_a : H^1(\omega_a) \rightarrow \mathcal{P}_0(\omega_a)$ is uniquely defined by $\int_{\omega_a} (v - P_a v) = 0$. Then, the Clément interpolation operator $I_0 : H_0^1(\Omega) \rightarrow V^h(\Omega) \cap H_0^1(\Omega)$ is defined by

$$I_0 v := \sum_{a \in \mathcal{N}_h^{\text{int}}} (P_a v)(a) \lambda_a,$$

and $I_B : H_B^1(\Omega) \rightarrow V^h(\Omega) \cap H_B^1(\Omega)$ by

$$I_B Q := \sum_{a \in \mathcal{N}_h^{\text{int}} \cup \mathcal{N}_N^{\text{ext}}} (P_a Q)(a) \lambda_a,$$

where λ_a is the (piecewise linear) basis function related to the vertex a , and $\mathcal{N}_N^{\text{ext}} := \{a \in \mathcal{N}_h^{\text{ext}}; a \in \Gamma_N\}$.

Finally, we state the anisotropic interpolation error estimates based on the alignment measure.

Lemma 2 *For all functions $v \in H_0^1(\Omega)$ and $Q \in H_B^1(\Omega)$, there hold*

$$\sum_{K \in \mathcal{T}_h} h_{\min,K}^{-2} \|v - I_0 v\|_K^2 \lesssim m_1(v, \mathcal{T}_h)^2 \|\nabla v\|^2, \tag{5}$$

$$\sum_{\sigma \in \mathcal{E}_h^{\text{int}}} \frac{h_\sigma}{h_{\min,\sigma}^2} \|v - I_0 v\|_\sigma^2 \lesssim m_1(v, \mathcal{T}_h)^2 \|\nabla v\|^2, \tag{6}$$

$$\sum_{K \in \mathcal{T}_h} h_{\min,K}^{-2} \|Q - I_B Q\|_K^2 \lesssim m_1(Q, \mathcal{T}_h)^2 \|\nabla Q\|^2, \tag{7}$$

$$\sum_{\sigma \in \mathcal{E}_h^{\text{int}} \cup \mathcal{E}_N^{\text{ext}}} \frac{h_\sigma}{h_{\min,\sigma}^2} \|Q - I_B Q\|_\sigma^2 \lesssim m_1(Q, \mathcal{T}_h)^2 \|\nabla Q\|^2, \tag{8}$$

where $\mathcal{E}_N^{\text{ext}} := \{\sigma \in \mathcal{E}_h^{\text{ext}}; \sigma \subset \Gamma_N\}$.

4 Residual error estimation

In this section, we present the residual error estimator for the conforming approximation (3) and show that it provides two-sided bounds on the error $\|(u - u_h, B - B_h)\|_W$ on anisotropic meshes.

Let (u_h, B_h) be the conforming finite element approximation. Here, we define the element residuals over an element K by

$$\begin{aligned} R_{1,K} &:= 1 + \Delta u_h + Ha \mathbf{a} \cdot \nabla B_h, \\ R_{2,K} &:= \Delta B_h + Ha \mathbf{a} \cdot \nabla u_h, \end{aligned}$$

and edge residuals by

$$\begin{aligned} R_{1,\sigma} &:= \begin{cases} \left[\left[\frac{\partial u_h}{\partial \mathbf{n}_\sigma} \right] \right], & \text{if } \sigma \in \mathcal{E}_h^{\text{int}}, \\ 0, & \text{others,} \end{cases} \\ R_{2,\sigma} &:= \begin{cases} \left[\left[\frac{\partial B_h}{\partial \mathbf{n}_\sigma} \right] \right], & \text{if } \sigma \in \mathcal{E}_h^{\text{int}} \cup \mathcal{E}_N^{\text{ext}}, \\ 0, & \text{others.} \end{cases} \end{aligned}$$

Obviously, $R_{1,K} = 1 + Ha \mathbf{a} \cdot \nabla B_h$ and $R_{2,K} = Ha \mathbf{a} \cdot \nabla u_h$ hold for piecewise linear functions as considered here.

The local residual error estimators $\eta_{1,K}$ and $\eta_{2,K}$ for an element K are defined by

$$\eta_{1,K} := h_{\min,K} \left(\|R_{1,K}\|_K^2 + \sum_{\sigma \subset \partial K} h_\sigma^{-1} \|R_{1,\sigma}\|_\sigma^2 \right)^{1/2}, \tag{9}$$

$$\eta_{2,K} := h_{\min,K} \left(\|R_{2,K}\|_K^2 + \sum_{\sigma \subset \partial K} h_\sigma^{-1} \|R_{2,\sigma}\|_\sigma^2 \right)^{1/2}, \tag{10}$$

and the global terms are

$$\eta_1^2 := \sum_{K \in \mathcal{T}_h} \eta_{1,K}^2, \quad \eta_2^2 := \sum_{K \in \mathcal{T}_h} \eta_{2,K}^2,$$

separately.

Theorem 3 *Let (u, B) be the weak solution of problem (1), and let (u_h, B_h) be the corresponding finite element approximation defined by (3). Then, the error is bounded globally from above by*

$$\|(u - u_h, B - B_h)\|_W \lesssim m_1(u - u_h, \mathcal{T}_h)\eta_1 + m_1(B - B_h, \mathcal{T}_h)\eta_2. \tag{11}$$

Proof For the convenience of expression, we set $e_u = u - u_h$ and $e_B = B - B_h$. Since $(\mathbf{a} \cdot \nabla e_B, e_u) = -(\mathbf{a} \cdot \nabla e_u, e_B)$, due to integration by parts, the Galerkin orthogonality and

Lemma 2 yield

$$\begin{aligned}
 & \| (e_u, e_B) \|_W^2 \\
 &= (\nabla e_u, \nabla (e_u - I_0 e_u)) - Ha(\mathbf{a} \cdot \nabla e_B, (e_u - I_0 e_u)) \\
 &\quad + (\nabla e_B, \nabla (e_B - I_B e_B)) - Ha(\mathbf{a} \cdot \nabla e_u, (e_B - I_B e_B)), \\
 y &= (1 + Ha \mathbf{a} \cdot \nabla B_h, e_u - I_0 e_u) - (\nabla u_h, \nabla (e_u - I_0 e_u)) \\
 &\quad + (Ha \mathbf{a} \cdot \nabla u_h, e_B - I_B e_B) - (\nabla B_h, \nabla (e_B - I_B e_B)), \\
 yy &= \sum_{K \in \mathcal{T}_h} (R_{1,K}, e_u - I_0 e_u) - \sum_{\sigma \in \mathcal{E}_h^{\text{int}}} \int_{\sigma} R_{1,\sigma} (e_u - I_0 e_u) \\
 &\quad + \sum_{K \in \mathcal{T}_h} (R_{2,K}, e_B - I_B e_B) - \sum_{\sigma \in \mathcal{E}_h^{\text{int}} \cup \mathcal{E}_N^{\text{ext}}} \int_{\sigma} R_{2,\sigma} (e_B - I_B e_B), \\
 y &\leq \left(\sum_{K \in \mathcal{T}_h} h_{\min,K}^2 \|R_{1,K}\|_K^2 \right)^{1/2} \left(\sum_{K \in \mathcal{T}_h} h_{\min,K}^{-2} \|e_u - I_0 e_u\|_K^2 \right)^{1/2} \\
 &\quad + \left(\sum_{\sigma \in \mathcal{E}_h^{\text{int}}} \frac{h_{\min,\sigma}^2}{h_{\sigma}} \|R_{1,\sigma}\|_{\sigma}^2 \right)^{1/2} \left(\sum_{\sigma \in \mathcal{E}_h^{\text{int}}} \frac{h_{\sigma}}{h_{\min,\sigma}^2} \|e_u - I_0 e_u\|_{\sigma}^2 \right)^{1/2} \\
 &\quad + \left(\sum_{K \in \mathcal{T}_h} h_{\min,K}^2 \|R_{2,K}\|_K^2 \right)^{1/2} \left(\sum_{K \in \mathcal{T}_h} h_{\min,K}^{-2} \|e_B - I_B e_B\|_K^2 \right)^{1/2} \\
 &\quad + \left(\sum_{\sigma \in \mathcal{E}_h^{\text{int}} \cup \mathcal{E}_N^{\text{ext}}} \frac{h_{\min,\sigma}^2}{h_{\sigma}} \|R_{2,\sigma}\|_{\sigma}^2 \right)^{1/2} \left(\sum_{\sigma \in \mathcal{E}_h^{\text{int}} \cup \mathcal{E}_N^{\text{ext}}} \frac{h_{\sigma}}{h_{\min,\sigma}^2} \|e_B - I_B e_B\|_{\sigma}^2 \right)^{1/2} \\
 &\lesssim m_1(e_u, \mathcal{T}_h) \eta_1 + m_1(e_B, \mathcal{T}_h) \eta_2,
 \end{aligned}$$

which concludes the proof.

Theorem 4 Under the assumption of Theorem 3, the error is bounded locally from below by

$$\eta_{1,K} \lesssim \|\nabla(u - u_h)\|_{\omega_K} + Ha \|B - B_h\|_{\omega_K}, \tag{12}$$

$$\eta_{2,K} \lesssim \|\nabla(B - B_h)\|_{\omega_K} + Ha \|u - u_h\|_{\omega_K} \tag{13}$$

for all $K \in \mathcal{T}_h$.

Proof The proof of lower error bounds needs to use the bubble functions and corresponding anisotropic inverse inequalities (see Lemma 1). Here, we only need to prove the lower bound (12). The remaining one can be derived analogously.

Observe $R_{1,K} = 1 + \Delta u_h + Ha \mathbf{a} \cdot \nabla B_h \in \mathcal{P}_0(K)$ and set

$$w_K := R_{1,K} b_K \in \mathcal{P}_3(K) \cap H_0^1(K).$$

The Cauchy-Schwarz inequality and integration by parts yield

$$\begin{aligned}
 \int_K R_{1,K} w_K &= (\nabla(u - u_h), \nabla w_K)_K - Ha(\mathbf{a} \cdot \nabla(B - B_h), w_K)_K \\
 &= (\nabla(u - u_h), \nabla w_K)_K + Ha(B - B_h, \mathbf{a} \cdot \nabla w_K)_K \\
 &\leq (\|\nabla(u - u_h)\|_K + Ha \|B - B_h\|_K) \|\nabla w_K\|_K.
 \end{aligned} \tag{14}$$

The inverse inequalities of Lemma 1 lead to

$$\begin{aligned}
 \int_K R_{1,K} w_K &= \|b_K^{1/2} R_{1,K}\|_K^2 \sim \|R_{1,K}\|_K^2, \\
 \|\nabla w_K\|_K &= \|\nabla(b_K R_{1,K})\|_K \lesssim h_{\min,K}^{-1} \|R_{1,K}\|_K,
 \end{aligned}$$

which, together with (14), result in

$$h_{\min,K} \|R_{1,K}\| \lesssim \|\nabla(u - u_h)\|_K + Ha \|B - B_h\|_K. \tag{15}$$

For an inner edge $\sigma \in \mathcal{E}_h^{\text{int}}$, set

$$w_\sigma := F_{\text{ext}}(R_{1,\sigma})b_\sigma \in \mathcal{P}_2(\omega_\sigma) \cap H_0^1(\omega_\sigma).$$

Integration by parts and (2) for $(v, Q) = (w_\sigma, 0)$ implies that

$$\begin{aligned} \int_\sigma w_\sigma R_{1,\sigma} &= \sum_{K \in \mathcal{T}_\sigma} \int_{\partial K} w_\sigma \frac{\partial u_h}{\partial \mathbf{n}_K} \\ &= \sum_{K \in \mathcal{T}_\sigma} ((\nabla u_h, \nabla w_\sigma)_K + (\Delta u_h, w_\sigma)_K) \\ &= \sum_{K \in \mathcal{T}_\sigma} (-(\nabla(u - u_h), \nabla w_\sigma)_K + Ha(\mathbf{a} \cdot \nabla(B - B_h), w_\sigma)_K + (R_K, w_\sigma)_K) \\ &= \sum_{K \in \mathcal{T}_\sigma} (-(\nabla(u - u_h), \nabla w_\sigma)_K - Ha(B - B_h, \mathbf{a} \cdot \nabla w_\sigma)_K + (R_K, w_\sigma)_K) \\ &\leq \sum_{K \in \mathcal{T}_\sigma} (\|\nabla(u - u_h)\|_K \|\nabla w_\sigma\|_K \\ &\quad + Ha \|B - B_h\|_K \|\nabla w_\sigma\|_K + \|R_K\|_K \|w_\sigma\|_K). \end{aligned} \tag{16}$$

Due to Lemma 1, we have the following relations:

$$\begin{aligned} \int_\sigma w_\sigma R_{1,\sigma} &= \|b_\sigma^{1/2} R_{1,\sigma}\|_\sigma^2 \sim \|R_{1,\sigma}\|_\sigma^2, \\ \|\nabla w_\sigma\|_L &= \|\nabla(F_{\text{ext}}(R_{1,\sigma})b_\sigma)\|_L \lesssim h_\sigma^{1/2} h_{\min,L}^{-1} \|R_{1,\sigma}\|_\sigma, \quad L \in \mathcal{T}_\sigma, \\ \|w_\sigma\|_L &= \|F_{\text{ext}}(R_{1,\sigma})b_\sigma\|_K \sim h_\sigma^{1/2} \|R_{1,\sigma}\|_\sigma, \quad L \in \mathcal{T}_\sigma, \end{aligned}$$

which, together with (15) and (16), lead to

$$h_{\min,K} h_\sigma^{-1} \|R_{1,\sigma}\|_\sigma \lesssim \|\nabla(u - u_h)\|_{\omega_\sigma} + Ha \|B - B_h\|_{\omega_\sigma}. \tag{17}$$

For an edge on the Dirichlet boundary, nothing needs to be done because $R_{1,\sigma} = 0$. Hence, combining (15) and (17), we conclude the lower error bound (12).

Remark 1 From Theorems 3 and 4, the lower bounds contain additional L^2 -error terms $Ha \|u - u_h\|_{\omega_K}$ and $Ha \|B - B_h\|_{\omega_K}$ that do not appear in the upper error bound (11). Therefore, the two-sided bounds on the error do not correspond completely. We point out that a very similar situation can be found for error estimators for the convection-diffusion problem^[10,22–23]. Moreover, only if the L^2 -error terms is dominated by the H^1 -error terms $\|\nabla(u - u_h)\|_{\omega_K}$ and $\|\nabla(B - B_h)\|_{\omega_K}$, the upper and lower bounds on the error will be of the same quality. Hence, the additional L^2 -error terms are mainly due to the H^1 -error terms, which is confirmed by our numerical experiments in the next section.

5 Numerical experiments

5.1 Anisotropic error indicator

Due to the large aspect ratio of anisotropic mesh, the alignment measure $m_1(\cdot, \mathcal{T}_h)$ enters the upper error bound in order to measure how well the alignment between the solution and

the mesh does in the sense: the worse the alignment is, the larger the alignment measure is. In other words, a sufficiently good mesh makes sure that the alignment measure is $\mathcal{O}(1)$, i.e.,

$$m_1(\cdot, \mathcal{T}_h) \sim 1. \tag{18}$$

In turn, the relation (18) can be used as a guide to design a proper anisotropic mesh. To this end, the definition (4) of the alignment measure $m_1(v, \mathcal{T}_h)$ is reformulated by

$$m_1(v, \mathcal{T}_h) := \left(\sum_{K \in \mathcal{T}_h} h_{\min,K}^{-2} \left(h_{\max,K}^2 \left\| \frac{\partial v}{\partial \mathbf{r}_1} \right\|_K^2 + h_{\min,K}^2 \left\| \frac{\partial v}{\partial \mathbf{r}_2} \right\|_K^2 \right) \right)^{1/2} / \|\nabla v\|, \tag{19}$$

where \mathbf{r}_1 and \mathbf{r}_2 are the corresponding unit vectors of \mathbf{p}_1 and \mathbf{p}_2 on each $K \in \mathcal{T}_h$, respectively, and so $C_K = (\mathbf{p}_1, \mathbf{p}_2) = (h_{\max,K} \mathbf{r}_1, h_{\min,K} \mathbf{r}_2)$. Therefore, the relation (18) holds, provided that

$$\sum_{K \in \mathcal{T}_h} h_{\max,K}^2 \left\| \frac{\partial v}{\partial \mathbf{r}_1} \right\|_K^2 \sim \sum_{K \in \mathcal{T}_h} h_{\min,K}^2 \left\| \frac{\partial v}{\partial \mathbf{r}_2} \right\|_K^2. \tag{20}$$

This formulation can be used to indicate the direction of adaptive mesh refinement. More specifically, due to (19), the upper error bound (11) holds as long as we have the following estimate:

$$\|(u - u_h, B - B_h)\|_W \lesssim \eta, \tag{21}$$

where

$$\begin{aligned} \eta^2 &:= (\eta^{(1)})^2 + (\eta^{(2)})^2, \\ (\eta^{(1)})^2 &:= \eta_1 \left(\sum_{K \in \mathcal{T}_h} \frac{h_{\max,K}^2}{h_{\min,K}^2} \left\| \frac{\partial(u - u_h)}{\partial \mathbf{r}_1} \right\|_K^2 \right)^{1/2} + \eta_2 \left(\sum_{K \in \mathcal{T}_h} \frac{h_{\max,K}^2}{h_{\min,K}^2} \left\| \frac{\partial(B - B_h)}{\partial \mathbf{r}_1} \right\|_K^2 \right)^{1/2}, \\ (\eta^{(2)})^2 &:= \eta_1 \left(\sum_{K \in \mathcal{T}_h} \left\| \frac{\partial(u - u_h)}{\partial \mathbf{r}_2} \right\|_K^2 \right)^{1/2} + \eta_2 \left(\sum_{K \in \mathcal{T}_h} \left\| \frac{\partial(B - B_h)}{\partial \mathbf{r}_2} \right\|_K^2 \right)^{1/2}. \end{aligned}$$

The relation (20) implies $\eta^{(1)} \sim \eta^{(2)}$. However, the estimate (21) is not available, because the exact solution (u, B) is usually unknown. To overcome this, we use the well-known Z-Z estimate^[6]. The gradient $(\nabla u, \nabla B)$ of the exact solution can be replaced by a recovered gradient $(\nabla^R u, \nabla^R B)$ by local averaging such as an approximate L^2 -projection of $(\nabla u_h, \nabla B_h)$ onto $V^h \times V^h$, i.e.,

$$\nabla^R u(a) := \frac{1}{|\omega_a|} \int_{\omega_a} \nabla u_h, \quad \nabla^R B(a) := \frac{1}{|\omega_a|} \int_{\omega_a} \nabla B_h, \quad a \in \mathcal{N}_h.$$

Numerical experiments in Ref. [24] showed that the averaging technique was quite more reliable on anisotropic meshes than expected. After this replacement, we introduce the global

anisotropic error indicator $\tilde{\eta}$ and the local anisotropic error indicator $\tilde{\eta}_K$ by

$$\begin{aligned} \tilde{\eta}^2 &:= \eta_1 \left(\sum_{K \in \mathcal{T}_h} \frac{h_{\max,K}^2}{h_{\min,K}^2} \|(\nabla^R u - \nabla u_h) \cdot \mathbf{r}_1\|_K^2 \right)^{1/2} \\ &\quad + \eta_2 \left(\sum_{K \in \mathcal{T}_h} \frac{h_{\max,K}^2}{h_{\min,K}^2} \|(\nabla^R B - \nabla B_h) \cdot \mathbf{r}_1\|_K^2 \right)^{1/2} \\ &\quad + \eta_1 \left(\sum_{K \in \mathcal{T}_h} \|(\nabla^R u - \nabla u_h) \cdot \mathbf{r}_2\|_K^2 \right)^{1/2} + \eta_2 \left(\sum_{K \in \mathcal{T}_h} \|(\nabla^R B - \nabla B_h) \cdot \mathbf{r}_2\|_K^2 \right)^{1/2}, \\ \tilde{\eta}_K^4 &:= (\tilde{\eta}_K^{(1)})^4 + (\tilde{\eta}_K^{(2)})^4, \\ (\tilde{\eta}_K^{(1)})^2 &:= \frac{h_{\max,K}}{h_{\min,K}} (\eta_{1,K} \|(\nabla^R u - \nabla u_h) \cdot \mathbf{r}_1\|_K + \eta_{2,K} \|(\nabla^R B - \nabla B_h) \cdot \mathbf{r}_1\|_K), \\ (\tilde{\eta}_K^{(2)})^2 &:= (\eta_{1,K} \|(\nabla^R u - \nabla u_h) \cdot \mathbf{r}_2\|_K + \eta_{2,K} \|(\nabla^R B - \nabla B_h) \cdot \mathbf{r}_2\|_K). \end{aligned}$$

In conclusion, the relation (18) implies that the adaptive algorithm should be designed such that the local anisotropic error indicators $\tilde{\eta}_K^{(1)}$ and $\tilde{\eta}_K^{(2)}$ satisfy, on each triangle K ,

$$(\tilde{\eta}_K^{(1)})^4 \sim (\tilde{\eta}_K^{(2)})^4 \sim \frac{1}{2} \tilde{\eta}_K^4.$$

5.2 Adaptive algorithm

We should implement an adaptive algorithm using the software FREEFEM++^[18] with the mesh generator Bamg^[19] based on a right metric field which will be built later. The goal of this adaptive algorithm is to generate a suitable anisotropic mesh so that the relative estimated error is close to a preset tolerance φ_{TOL} , i.e.,

$$0.75\varphi_{\text{TOL}} \leq \frac{\tilde{\eta}}{\|(u_h, B_h)\|_W} \leq 1.25\varphi_{\text{TOL}}.$$

A sufficient condition to generate such an anisotropic mesh is to make sure that for all $K \in \mathcal{T}_h$, it holds

$$\frac{1}{|\mathcal{T}_h|} 0.75^2 \varphi_{\text{TOL}}^2 \|(u_h, B_h)\|_W^2 \leq \tilde{\eta}_K^2 \leq \frac{1}{|\mathcal{T}_h|} 1.25^2 \varphi_{\text{TOL}}^2 \|(u_h, B_h)\|_W^2, \tag{22}$$

where $|\mathcal{T}_h|$ denotes the number of elements in \mathcal{T}_h , as well as the number $|\mathcal{N}_h|$ of mesh vertices which will be used later. In order to get data at the mesh vertices, at each vertex a , we introduce the anisotropic error indicator $\tilde{\eta}_a$ defined by

$$\tilde{\eta}_a := \left(\sum_{K \in \mathcal{T}_a} \tilde{\eta}_K^4 \right)^{1/4}.$$

Since

$$\sum_{a \in \mathcal{N}_h} \tilde{\eta}_a^4 = 3 \sum_{K \in \mathcal{T}_h} \tilde{\eta}_K^4,$$

there holds (22), whenever we generate a mesh satisfying, for all vertices $a \in \mathcal{N}_h$,

$$\frac{3}{|\mathcal{N}_h|^2} 0.75^4 \varphi_{\text{TOL}}^4 \|(u_h, B_h)\|_W^4 \leq \tilde{\eta}_a^4 \leq \frac{3}{|\mathcal{N}_h|^2} 1.25^4 \varphi_{\text{TOL}}^4 \|(u_h, B_h)\|_W^4.$$

With the mesh generator Bamg, the metric field \mathcal{M} is needed to be given at each vertex a as continuous \mathcal{P}_1 finite element functions, namely, the two eigenvalues $\lambda_{1,a}, \lambda_{2,a}$ ($\lambda_{1,a} \leq \lambda_{2,a}$) and the corresponding eigenvectors $\mathbf{r}_{1,a}, \mathbf{r}_{2,a}$ such that $\mathcal{M} = R^T \Lambda R$, where

$$R(a) := (\mathbf{r}_{1,a}, \mathbf{r}_{2,a}), \quad \Lambda(a) := \begin{bmatrix} \lambda_{1,a} & 0 \\ 0 & \lambda_{2,a} \end{bmatrix}.$$

Then, in a vicinity of the vertex a , the wanted mesh size can be defined by the metric field \mathcal{M} such that the size h is equal to $|\mathbf{x}|/\sqrt{\mathbf{x}^T \mathcal{M}(a) \mathbf{x}}$ in the direction $\mathbf{x} \in \mathbb{R}^2$, where $|\mathbf{x}| := \sqrt{\mathbf{x}^T \mathbf{x}}$.

Then, the adaptive algorithm is designed. First, the values $\tilde{\eta}_a^{(1)}$ and $\tilde{\eta}_a^{(2)}$ at all the vertices a of the mesh are defined by

$$\tilde{\eta}_a^{(1)} := \left(\sum_{K \in \mathcal{T}_a} (\tilde{\eta}_K^{(1)})^4 \right)^{1/4}, \quad \tilde{\eta}_a^{(2)} := \left(\sum_{K \in \mathcal{T}_a} (\tilde{\eta}_K^{(2)})^4 \right)^{1/4}.$$

Thus, the error at each vertex a in the direction of maximum stretching can be represented by $\tilde{\eta}_a^{(1)}$, whereas the error at each vertex a in the direction of minimum stretching is denoted by $\tilde{\eta}_a^{(2)}$. Second, we compute the value of mesh size $h_{1,a}$ ($h_{2,a}$) for all vertices $a \in \mathcal{N}_h$ by averaging all the values $h_{\max,K}$ ($h_{\min,K}$) corresponding to the neighboring triangles K in \mathcal{T}_a . The algorithm is carried out as follows. For $i = 1, 2$, if

$$2(\tilde{\eta}_a^{(i)})^4 < \frac{3}{|\mathcal{N}_h|^2} 0.75^4 \varphi_{\text{TOT}}^4 \|(u_h, B_h)\|_W^4,$$

then the value of $\lambda_{i,a}$ is set to $(\frac{3}{2}h_{i,a})^{-1}$. If

$$2(\tilde{\eta}_a^{(i)})^4 > \frac{3}{|\mathcal{N}_h|^2} 1.25^4 \varphi_{\text{TOT}}^4 \|(u_h, B_h)\|_W^4,$$

then the value of $\lambda_{i,a}$ is set to be $(\frac{2}{3}h_{i,a})^{-1}$. Otherwise, $\lambda_{i,a}$ is set to be $h_{i,a}^{-1}$. Finally, for all vertices $a \in \mathcal{N}_h$, let $\mathbf{r}_{1,a}$ and $\mathbf{r}_{2,a}$ be, respectively, the unit eigenvectors corresponding to the smallest and largest eigenvalues of the Z-Z estimates \tilde{G}_a of the error gradient matrix defined by an average

$$\tilde{G}_a := \frac{1}{|\mathcal{T}_a|} \int_{\omega_a} (\nabla^R u - \nabla u_h)(\nabla^R u - \nabla u_h)^T + \frac{1}{|\mathcal{T}_a|} \int_{\omega_a} (\nabla^R B - \nabla B_h)(\nabla^R B - \nabla B_h)^T.$$

With the resulting metric \mathcal{M} , we build a new anisotropic mesh using Bamg, which should insure $m_1^R(u - u_h, \mathcal{T}_h) \sim 1$ and $m_1^R(B - B_h, \mathcal{T}_h) \sim 1$, where $m_1^R(u - u_h, \mathcal{T}_h)$ and $m_1^R(B - B_h, \mathcal{T}_h)$ are the Z-Z estimates of $m_1(u - u_h, \mathcal{T}_h)$ and $m_1(B - B_h, \mathcal{T}_h)$ obtained by replacing the gradient $(\nabla u, \nabla B)$ of the exact solution by the recovered one $(\nabla^R u, \nabla^R B)$, i.e.,

$$m_1^R(u - u_h, \mathcal{T}_h) := \frac{\left(\sum_{K \in \mathcal{T}_h} h_{\min,K}^{-2} \|C_K^T (\nabla^R u - \nabla u_h)\|_K^2 \right)^{1/2}}{\|\nabla^R u - \nabla u_h\|},$$

$$m_1^R(B - B_h, \mathcal{T}_h) := \frac{\left(\sum_{K \in \mathcal{T}_h} h_{\min,K}^{-2} \|C_K^T (\nabla^R B - \nabla B_h)\|_K^2 \right)^{1/2}}{\|\nabla^R B - \nabla B_h\|},$$

respectively. According to the numerical results of the next subsection, it always holds that both $m_1^R(u - u_h, \mathcal{T}_h)$ and $m_1^R(B - B_h, \mathcal{T}_h)$ are close to 1, which indicates that the anisotropy of meshes is well adapted to the exact solution of the problem. Therefore, an efficient error estimation is to be expected. In the future, we plan to extend such an efficient anisotropic adaptive FEM to other problems, e.g., nonconforming FEMs^[25–26] for fourth-order elliptic singular perturbation problems with boundary layers^[27].

5.3 Numerical results

In this subsection, for the three test problems, a series of numerical simulations are performed by the anisotropic adaptive FEM developed in this paper. In all the test problems, we consider the domain $\Omega = (0, 1) \times (0, 1)$ and set the tolerance $\varphi_{\text{TOL}} = 0.01$.

Example 1 (The Shercliff problem) For this example, there exists an analytic solution, and the numerical data are available in Refs. [1] and [2] such that a comparison can be done between the approximate solution and the exact solution. Here, the walls of the channel are insulated ($B = 0$ on $\partial\Omega$), and on the solid walls, the velocity is zero ($u = 0$ on $\partial\Omega$). The external magnetic field B_0 is applied in the x -axis ($\alpha = 0$) (see Fig. 2).

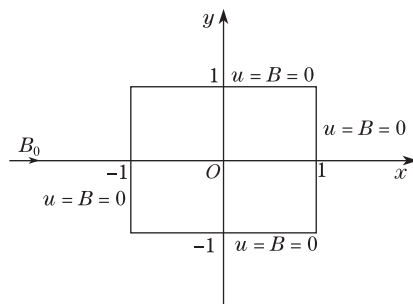


Fig. 2 Boundary conditions of Shercliff problem

For the Hartmann numbers $Ha = 100$ and $Ha = 500$, the comparisons are done between the approximate solution (u_h, B_h) and the exact solution (u, B) in Tables 1 and 2, respectively. One can see that two results are comparable. In addition, Table 3 presents the corresponding mesh information and Z - Z estimates of the alignment measures after some iterations during the adaptation process. For the sake of comparison, the corresponding meshes and contour plots for approximate solutions are shown in Figs. 3–4 for $Ha = 100$ and $Ha = 500$, respectively. It is worth mentioning that the use of anisotropic adaptive FEM can capture the boundary or interior layers in some directions and allow the number of vertices dramatically reduced for a given level of accuracy. In the next two examples, the superior performance will be further demonstrated for much larger Hartmann numbers, such as 10^3 , 10^4 , and 10^5 .

Table 1 Approximate and exact solutions for Shercliff problem at $Ha = 100$

x	y	u_h	u	B_h	B
0.00	0.00	0.010 000 0	0.010 000 0	0.000 000 0	0.000 000 0
0.25	0.00	0.010 000 0	0.010 000 0	-0.002 500 0	-0.002 500 0
0.50	0.00	0.010 000 0	0.010 000 0	-0.005 000 0	-0.005 000 0
0.75	0.00	0.010 000 0	0.010 000 0	-0.007 500 0	-0.007 500 0
0.00	0.25	0.010 000 0	0.010 000 0	0.000 000 0	0.000 000 0
0.25	0.25	0.010 000 0	0.010 000 0	-0.002 500 0	-0.002 500 0
0.50	0.25	0.010 000 0	0.010 000 0	-0.005 000 0	-0.005 000 0
0.75	0.25	0.010 000 0	0.009 999 9	-0.007 500 0	-0.007 499 9
0.00	0.50	0.009 999 5	0.009 999 2	0.000 000 0	0.000 000 0
0.25	0.50	0.009 998 3	0.009 998 1	-0.002 498 2	-0.002 498 2
0.50	0.50	0.009 994 6	0.009 994 4	-0.004 994 6	-0.004 994 4
0.75	0.50	0.009 987 0	0.009 986 8	-0.007 487 0	-0.007 486 8
0.00	0.75	0.009 761 3	0.009 761 4	0.000 000 0	0.000 000 0
0.25	0.75	0.009 715 8	0.009 716 3	-0.002 303 3	-0.002 303 0
0.50	0.75	0.009 585 5	0.009 585 8	-0.004 602 3	-0.004 602 4
0.75	0.75	0.009 387 2	0.009 386 3	-0.006 887 6	-0.006 886 9

Table 2 Approximate and exact solutions for Shercliff problem at $Ha = 500$

x	y	u_h	u	B_h	B
0.00	0.00	0.002 000 0	0.002 000 0	0.000 000 0	0.000 000 0
0.25	0.00	0.002 000 0	0.002 000 0	-0.000 500 0	-0.000 500 0
0.50	0.00	0.002 000 0	0.002 000 0	-0.000 999 9	-0.001 000 0
0.75	0.00	0.002 000 0	0.002 000 0	-0.001 500 0	-0.001 500 0
0.00	0.25	0.002 000 0	0.002 000 0	0.000 000 0	0.000 000 0
0.25	0.25	0.002 000 0	0.002 000 0	-0.000 500 0	-0.000 500 0
0.50	0.25	0.002 000 0	0.002 000 0	-0.001 000 0	-0.001 000 0
0.75	0.25	0.002 000 0	0.002 000 0	-0.001 500 0	-0.001 500 0
0.00	0.50	0.002 000 0	0.002 000 0	0.000 000 0	0.000 000 0
0.25	0.50	0.002 000 0	0.002 000 0	-0.000 500 0	-0.000 500 0
0.50	0.50	0.002 000 0	0.002 000 0	-0.001 000 0	-0.001 000 0
0.75	0.50	0.002 000 0	0.002 000 0	-0.001 500 0	-0.001 500 0
0.00	0.75	0.002 000 1	0.002 000 0	0.000 000 0	0.000 000 0
0.25	0.75	0.001 999 9	0.001 999 9	-0.000 499 9	-0.000 499 9
0.50	0.75	0.001 999 7	0.001 999 7	-0.000 999 7	-0.000 999 7
0.75	0.75	0.001 999 1	0.001 999 2	-0.001 499 1	-0.001 499 2

Table 3 Mesh information and Z-Z estimates of alignment measures for Shercliff problem

Ha	Number of vertices	Maximal aspect ratio	$m_1^R(u - u_h, \mathcal{T}_h)$	$m_1^R(B - B_h, \mathcal{T}_h)$
100	37 266	5.3×10^3	1.36	1.41
500	21 799	3.7×10^4	1.36	1.40

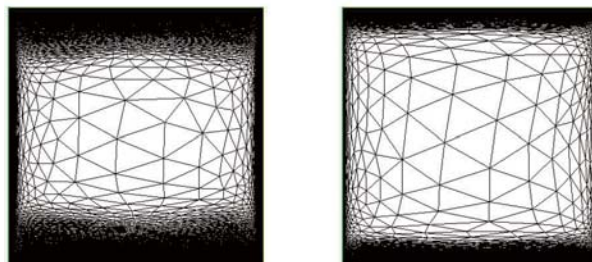


Fig. 3 Corresponding meshes for Shercliff problem at $Ha = 100$ (left) and $Ha = 500$ (right)

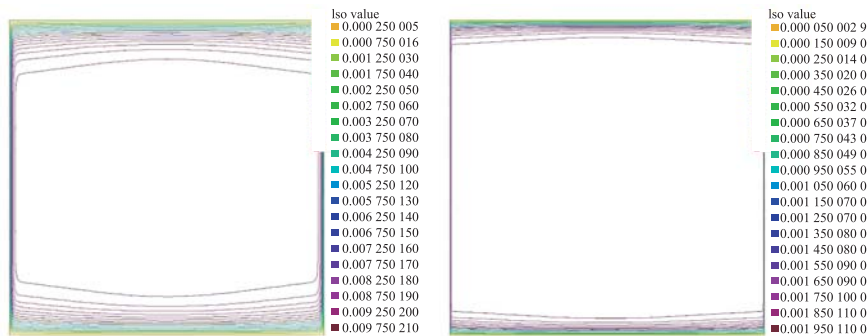


Fig. 4 Approximate velocity fields for Shercliff problem at $Ha = 100$ (left) and $Ha = 500$ (right)

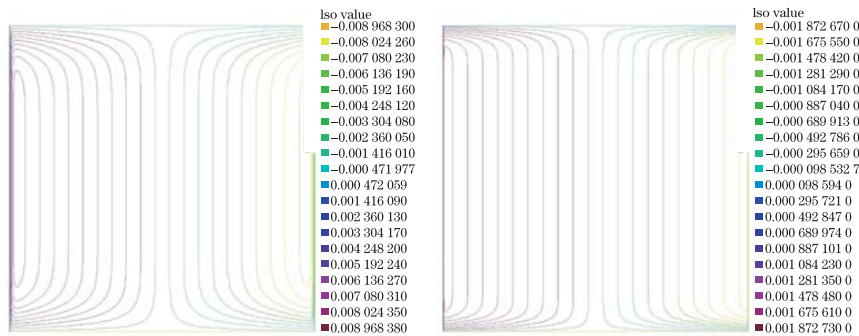


Fig. 5 Approximate magnetic fields for Shercliff problem at $Ha = 100$ (left) and $Ha = 500$ (right)

Example 2 (The two-dimensional square-channel flow with an oblique applied magnetic field) The same MHD problem as Example 1 is considered, except that the externally applied magnetic field B_0 has various positive angles α with the x -axis (see Fig. 6). Here, for the values of $\alpha = 0, \pi/4$, and $\pi/3$, numerical computations are carried out at different Hartmann numbers. The resulting meshes and contour plots for approximate solutions generated by the anisotropic adaptive FEM are presented at Hartmann numbers $Ha = 10^3, 10^4$, and 10^5 , respectively, in Figs. 7–15. The numerical results show that when Hartmann number increases, the boundary or interior layers are well dealt with by anisotropic meshes. The corresponding mesh information and approximate alignment measures are presented in Tables 4–6.

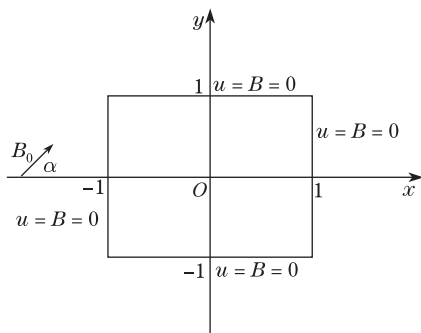


Fig. 6 Boundary conditions of Example 2

Table 4 Mesh information and Z-Z estimates of alignment measures for Example 2 at $Ha = 10^3$

α	Number of vertices	Maximal aspect ratio	$m_1^R(u - u_h, \mathcal{T}_h)$	$m_1^R(B - B_h, \mathcal{T}_h)$
0	19 950	7.4×10^4	1.38	1.40
$\pi/4$	43 135	4.1×10^3	1.34	1.34
$\pi/3$	42 652	2.9×10^4	1.35	1.35

Table 5 Mesh information and Z-Z estimates of alignment measures for Example 2 at $Ha = 10^4$

α	Number of vertices	Maximal aspect ratio	$m_1^R(u - u_h, \mathcal{T}_h)$	$m_1^R(B - B_h, \mathcal{T}_h)$
0	65 502	9.7×10^5	1.31	1.33
$\pi/4$	68 042	1.1×10^5	1.36	1.36
$\pi/3$	63 904	4.5×10^4	1.32	1.32

Table 6 Mesh information and Z-Z estimates of alignment measures for Example 2 at $Ha = 10^5$

α	Number of vertices	Maximal aspect ratio	$m_1^R(u - u_h, \mathcal{T}_h)$	$m_1^R(B - B_h, \mathcal{T}_h)$
0	134 734	2.1×10^6	1.27	1.28
$\pi/4$	107 130	2.7×10^5	1.27	1.28
$\pi/3$	102 643	1.9×10^6	1.26	1.26

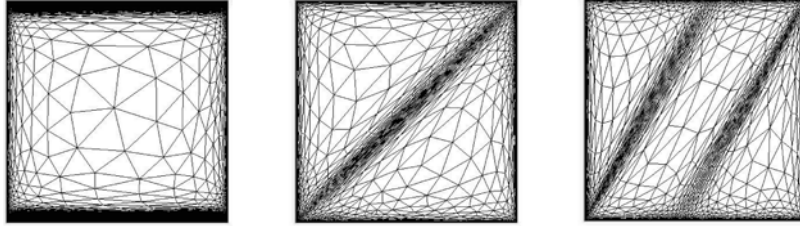


Fig. 7 Corresponding meshes for Example 2 at $Ha = 10^3$ with $\alpha = 0$ (left), $\alpha = \pi/4$ (middle), and $\alpha = \pi/3$ (right)

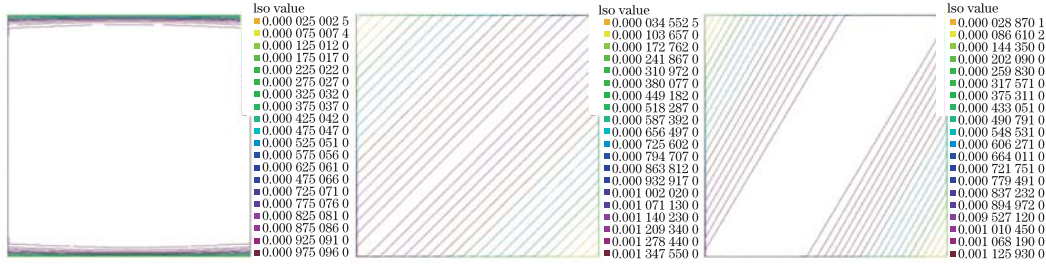


Fig. 8 Approximate velocity fields for Example 2 at $M = 10^3$ with $\alpha = 0$ (left), $\alpha = \pi/4$ (middle), and $\alpha = \pi/3$ (right)

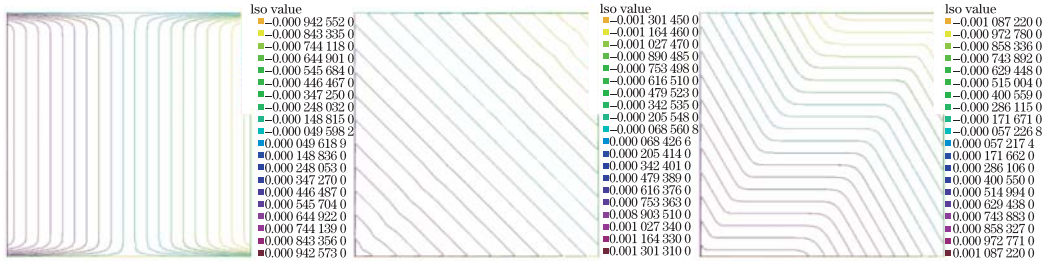


Fig. 9 Approximate magnetic fields for Example 2 at $M = 10^3$ with $\alpha = 0$ (left), $\alpha = \pi/4$ (middle), and $\alpha = \pi/3$ (right)

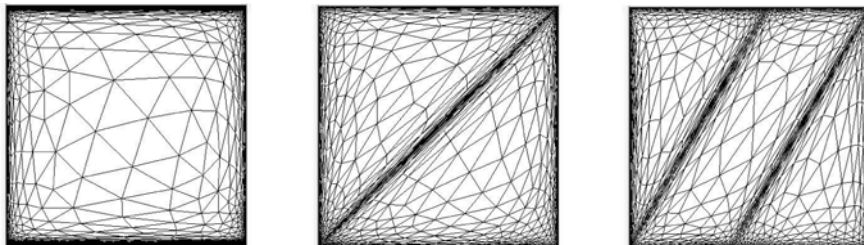


Fig. 10 Corresponding meshes for Example 2 at $Ha = 10^4$ with $\alpha = 0$ (left), $\alpha = \pi/4$ (middle), and $\alpha = \pi/3$ (right)



Fig. 11 Approximate velocity fields for Example 2 at $Ha = 10^4$ with $\alpha = 0$ (left), $\alpha = \pi/4$ (middle), and $\alpha = \pi/3$ (right)

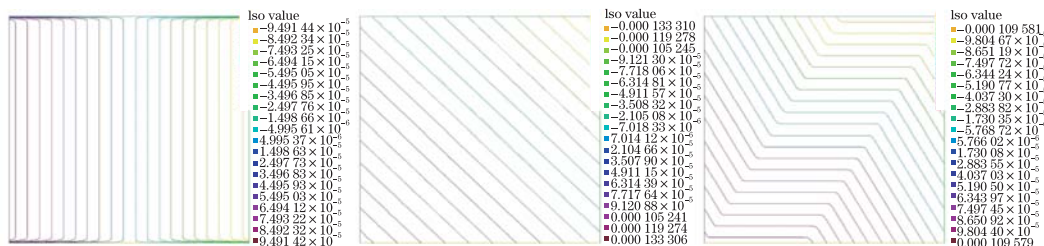


Fig. 12 Approximate magnetic fields for Example 2 at $Ha = 10^4$ with $\alpha = 0$ (left), $\alpha = \pi/4$ (middle), and $\alpha = \pi/3$ (right)

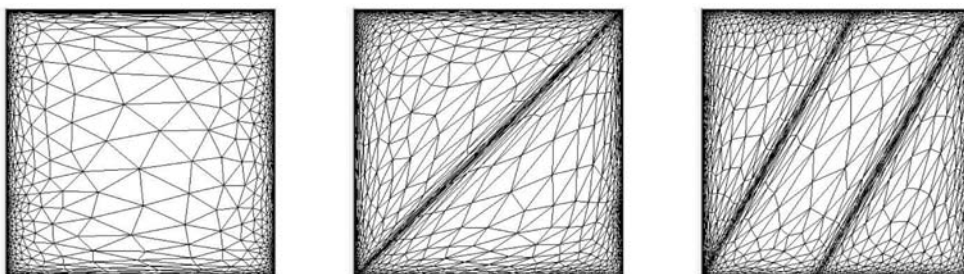


Fig. 13 Corresponding meshes for Example 2 at $Ha = 10^5$ with $\alpha = 0$ (left), $\alpha = \pi/4$ (middle), and $\alpha = \pi/3$ (right)

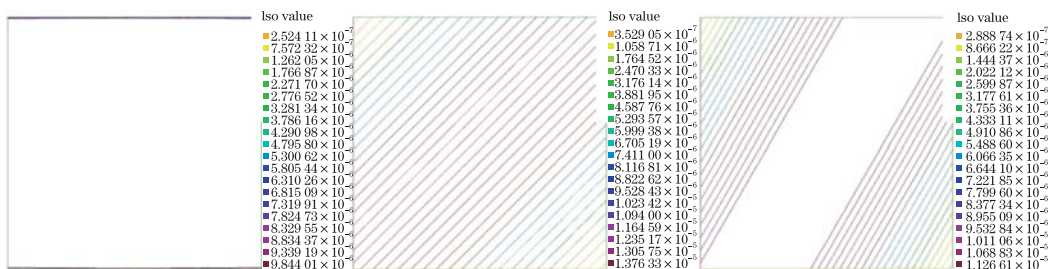


Fig. 14 Approximate velocity fields for Example 2 at $Ha = 10^5$ with $\alpha = 0$ (left), $\alpha = \pi/4$ (middle), and $\alpha = \pi/3$ (right)

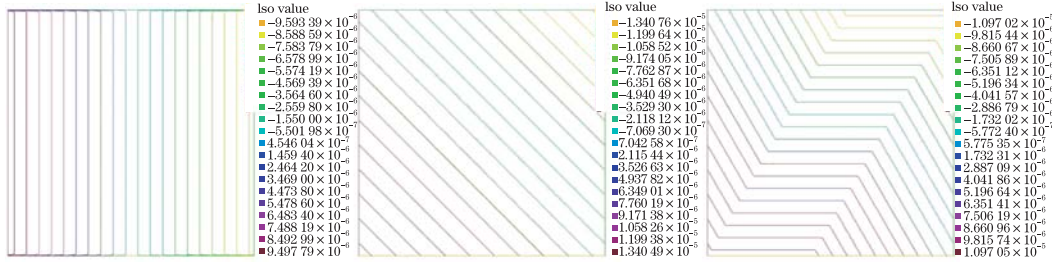


Fig. 15 Approximate magnetic fields for Example 2 at $Ha = 10^5$ with $\alpha = 0$ (left), $\alpha = \pi/4$ (middle), and $\alpha = \pi/3$ (right)

Example 3 (The two-dimensional square-channel flow with a partly conducting boundary) Here, the external magnetic field B_0 is perpendicular to the wall at $x = -1$ (i.e., $\alpha = 0$). For a length $2l$ at the center, the wall is electrically insulated (see Fig. 16). In Figs. 17–25, the anisotropic meshes and contour plots for approximate solutions are presented for $l = 0.2, 0.5,$ and 0.7 at different Hartmann numbers ($Ha = 10^3, 10^4,$ and 10^5), respectively. The corresponding mesh information and approximate alignment measures are presented in Tables 7–9.

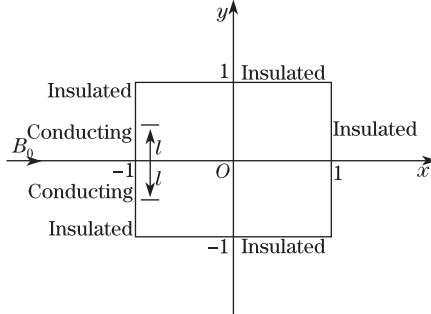


Fig. 16 Boundary conditions of Example 3

Table 7 Mesh information and Z-Z estimates of alignment measures for Example 3 at $Ha = 10^3$

l	Number of vertices	Maximal aspect ratio	$m_1^R(u - u_h, T_h)$	$m_1^R(B - B_h, T_h)$
0.2	66 753	3.3×10^4	1.37	1.39
0.5	82 971	1.7×10^4	1.38	1.41
0.7	107 763	1.3×10^4	1.38	1.41

Table 8 Mesh information and Z-Z estimates of alignment measures for Example 3 at $Ha = 10^4$

l	Number of vertices	Maximal aspect ratio	$m_1^R(u - u_h, T_h)$	$m_1^R(B - B_h, T_h)$
0.2	66 662	2.1×10^5	1.33	1.35
0.5	72 563	1.4×10^5	1.34	1.36
0.7	83 369	7.9×10^4	1.36	1.38

Table 9 Mesh information and Z-Z estimates of alignment measures for Example 3 at $Ha = 10^5$

l	Number of vertices	Maximal aspect ratio	$m_1^R(u - u_h, T_h)$	$m_1^R(B - B_h, T_h)$
0.2	107 933	1.5×10^6	1.28	1.30
0.5	101 330	9.4×10^5	1.29	1.31
0.7	118 050	6.1×10^5	1.30	1.32

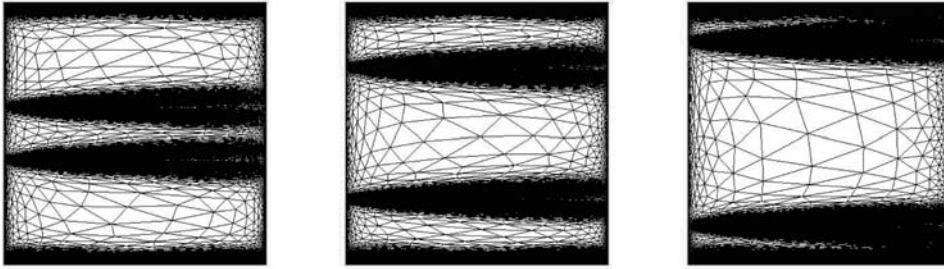


Fig. 17 Corresponding meshes for Example 3 at $Ha = 10^3$ with $l = 0.2$ (left), $l = 0.5$ (middle), and $l = 0.7$ (right)

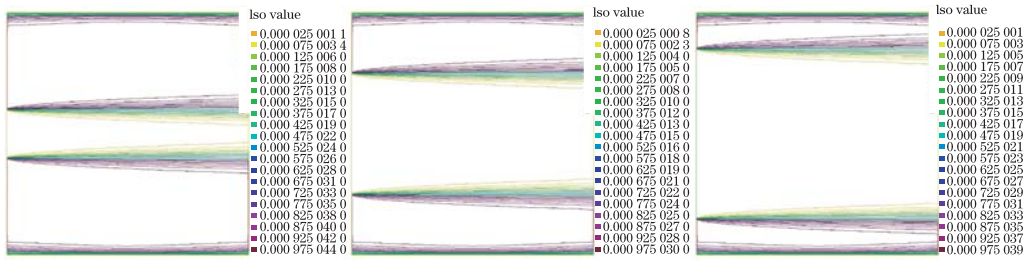


Fig. 18 Approximate velocity fields for Example 3 at $Ha = 10^3$ with $l = 0.2$ (left), $l = 0.5$ (middle), and $l = 0.7$ (right)

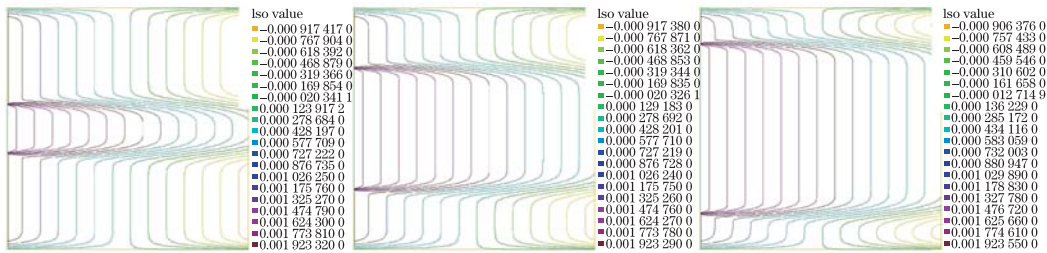


Fig. 19 Approximate magnetic fields for Example 3 at $Ha = 10^3$ with $l = 0.2$ (left), $l = 0.5$ (middle), and $l = 0.7$ (right)

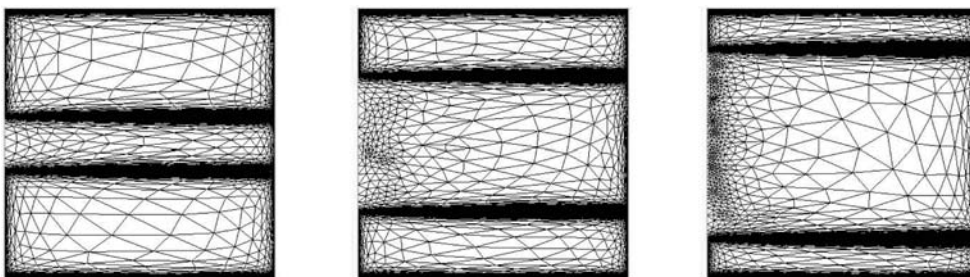


Fig. 20 Corresponding meshes for Example 3 at $Ha = 10^4$ with $l = 0.2$ (left), $l = 0.5$ (middle), and $l = 0.7$ (right)

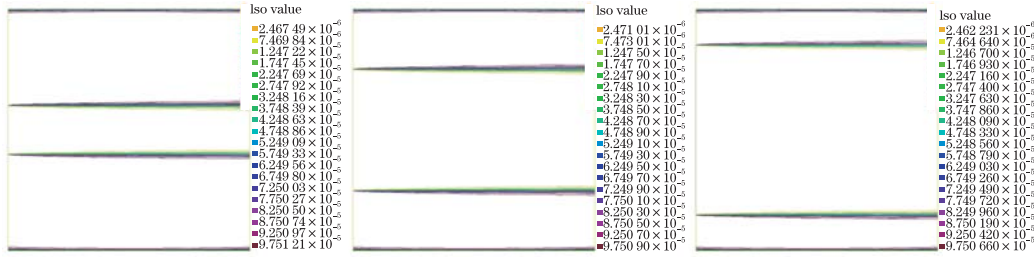


Fig. 21 Approximate velocity fields for Example 3 at $Ha = 10^4$ with $l = 0.2$ (left), $l = 0.5$ (middle), and $l = 0.7$ (right)

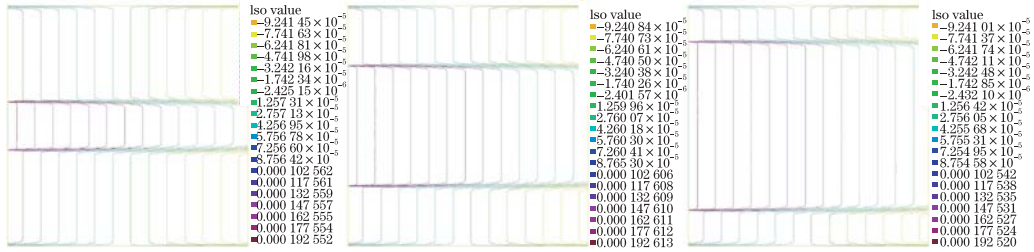


Fig. 22 Approximate magnetic fields for Example 3 at $Ha = 10^4$ with $l = 0.2$ (left), $l = 0.5$ (middle), and $l = 0.7$ (right)

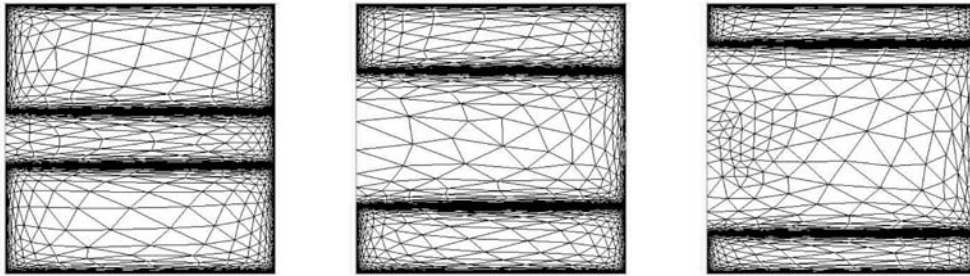


Fig. 23 Corresponding meshes for Example 3 at $Ha = 10^5$ with $l = 0.2$ (left), $l = 0.5$ (middle), and $l = 0.7$ (right)

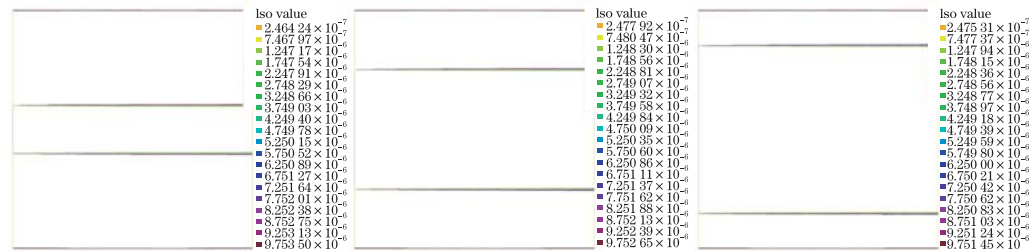


Fig. 24 Approximate velocity fields for Example 3 at $Ha = 10^5$ with $l = 0.2$ (left), $l = 0.5$ (middle), and $l = 0.7$ (right)

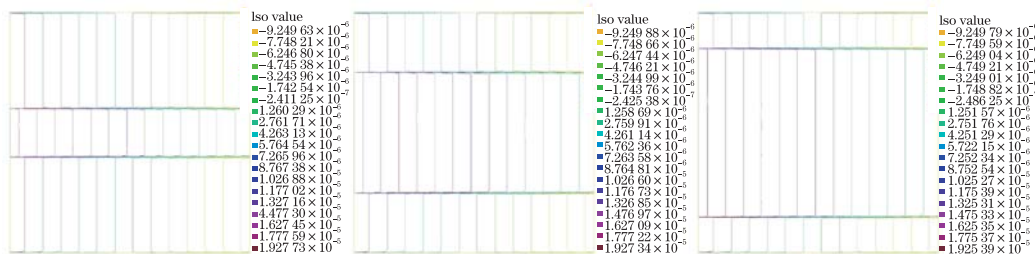


Fig. 25 Approximate magnetic fields for Example 3 at $Ha = 10^5$ with $l = 0.2$ (left), $l = 0.5$ (middle), and $l = 0.7$ (right)

6 Conclusions

In this paper, an anisotropic adaptive FEM is proposed to solve the MHD duct flow at high Hartmann numbers. The most distinguish feature of this method is that the layer information from some directions is captured well such that the number of mesh vertices is dramatically reduced for a given level of accuracy. Further, an adaptive algorithm is implemented for several examples on a rectangular domain, where it is shown that even for high values of the Hartmann number, this method gives accurate and stable results. Finally, we note that the anisotropic adaptive FEM can be applied to channels with arbitrary cross-sections.

References

- [1] Nesliturk, A. I. and Tezer-Sezgin, M. The finite element method for MHD flow at high Hartmann numbers. *Comput. Methods Appl. Mech. Engrg.*, **194**(9-11), 1201–1224 (2005)
- [2] Hsieh, P. W. and Yang, S. Y. A bubble-stabilized least-squares finite element method for steady MHD duct flow problems at high Hartmann numbers. *J. Comput. Phys.*, **228**(22), 8301–8320 (2009)
- [3] Hsieh, P. W., Shih, Y., and Yang, S. Y. A tailored finite point method for solving steady MHD duct flow problems with boundary layers. *Commun. Comput. Phys.*, **10**(1), 161–182 (2011)
- [4] Hosseinzadeh, H., Dehghan, M., and Mirzaei, D. The boundary elements method for magneto-hydrodynamic (MHD) channel flows at high Hartmann numbers. *Appl. Math. Model.*, **37**(4), 2337–2351 (2013)
- [5] Zhang, L., Ouyang, J., and Zhang, X. The two-level element free Galerkin method for MHD flow at high Hartmann numbers. *Phys. Lett. A*, **372**(35), 5625–5638 (2008)
- [6] Ainsworth, M. and Oden, J. T. *A Posteriori Error Estimation in Finite Element Analysis*, John Wiley & Sons, New York (2000)
- [7] Verfürth, R. *A Review of a Posteriori Error Estimation and Adaptive Mesh-Refinement Techniques*, Teubner-Wiley, Stuttgart (1996)
- [8] Kunert, G. *A Posteriori Error Estimation for Anisotropic Tetrahedral and Triangular Finite Element Meshes*, Ph. D. dissertation, Chemnitz University of Technology (1999)
- [9] Kunert, G. A posteriori residual error estimator for the finite element method on anisotropic tetrahedral meshes. *Numer. Math.*, **86**(3), 471–490 (2000)
- [10] Kunert, G. A posteriori error estimation for convection dominated problems on anisotropic meshes. *Math. Method. Appl. Sci.*, **26**(7), 589–617 (2003)
- [11] Frey, P. J. and Alauzet, F. Anisotropic mesh adaptation for CFD computations. *Comput. Methods Appl. Mech. Engrg.*, **194**(48-49), 5068–5082 (2005)
- [12] Dolejší, V. Anisotropic mesh adaptation for finite volume and finite element methods on triangular meshes. *Comput. Visual. Sci.*, **1**(3), 165–178 (1998)
- [13] Apel, T. *Anisotropic Finite Elements: Local Estimates and Applications*, Teubner, Stuttgart (1999)

-
- [14] Chen, S. and Xiao, L. Interpolation theory of anisotropic finite elements and applications. *Sci. China Ser. A*, **51**(8), 1361–1375 (2008)
- [15] Picasso, M. An anisotropic error indicator based on Zienkiewicz-Zhu error estimator: application to elliptic and parabolic problems. *SIAM J. Sci. Comput.*, **24**(4), 1328–1355 (2003)
- [16] Formaggia, L., Micheletti, S., and Perotto, S. Anisotropic mesh adaption in computational fluid dynamics: application to the advection-diffusion-reaction and the Stokes problems. *Appl. Numer. Math.*, **51**(4), 511–533 (2004)
- [17] Kuate, R. Anisotropic metrics for finite element meshes using a posteriori error estimates: Poisson and Stokes equations. *Eng. Comput. -Germany*, **29**(4), 497–505 (2013)
- [18] Hecht, F., Pironneau, O., Morice, J., Le Hyaric, A., and Ohtsuka, K. Freefem++ documentation, version 3.19-1. <http://www.freefem.org/ff++> (2012)
- [19] Hecht, F. Bamg: bidimensional anisotropic mesh generator. <http://www-rocq1.inria.fr/gamma/cdrom/www/bamg/eng.htm> (1998)
- [20] Scanduzzi, R. and Schrefler, B. FEM in steady MHD duct flow problems. *Int. J. Numer. Meth. Engrg.*, **30**(4), 647–659 (1990)
- [21] Meir, A. Finite element analysis of magnetohydrodynamic pipe flow. *Appl. Math. Comput.*, **57**(2), 177–196 (1993)
- [22] Kay, D. The reliability of local error estimators for convection-diffusion equations. *IMA J. Numer. Anal.*, **21**(1), 107–122 (2001)
- [23] Verfürth, R. A posteriori error estimators for convection-diffusion equations. *Numer. Math.*, **80**(4), 641–663 (1998)
- [24] Babuška, I., Strouboulis, T., Upadhyay, C. S., Gangaraj, S. K., and Copps, K. Validation of a posteriori error estimators by numerical approach. *Int. J. Numer. Meth. Engrg.*, **37**(7), 1073–1123 (1994)
- [25] Chen, H., Chen, S., and Qiao, Z. C^0 -nonconforming tetrahedral and cuboid elements for the three-dimensional fourth order elliptic problem. *Numer. Math.*, **124**(1), 99–119 (2013)
- [26] Chen, H. R., Chen, S. C., and Qiao, Z. H. C^0 -nonconforming triangular prism elements for the three-dimensional fourth order elliptic problem. *J. Sci. Comput.*, **55**(3), 645–658 (2013)
- [27] Chen, H. and Chen, S. Uniformly convergent nonconforming element for 3-D fourth order elliptic singular perturbation problem. *J. Comput. Math.*, **32**(6), 687–695 (2014)